ACS APPLIED NANO MATERIALS

www.acsanm.org

Article

Plasmonic Absorption in Antigen-Induced Aggregated Gold Nanoparticles: Toward a Figure of Merit for Optical Nanosensors

Carlo Bravin and Vincenzo Amendola*

Cite This: *ACS Appl. Nano Mater.* 2022, 5, 578−586

Read Online

ACCESS | Metrics & More | Article Recommendations | Supporting Information

ABSTRACT: Gold nanoparticles (Au NPs) have been extensively used for colorimetric and optical detection of various analytes, exploiting the difference in optical properties when the NPs are dispersed or aggregated. The properties of Au NPs-based optical sensors depend strongly on the particle size, spacing, number, and disposition in the aggregate, which explains the different performances reported so far for this class of sensors. Here, we investigated the optical response of a model Au NP immunosensor and the correlation of its plasmonic absorption with the analyte-dependent aggregation state, supported by transmission electron microscopy and numerical calculations. The antigen−antibody system used for this study is the C-reactive protein (CRP)/anti-CRP couple, well-established and of great applicative interest. The results provide several insights into the evaluation of the extent and type of antigen-induced aggregation for receptor-conjugated Au NPs and point toward the identification of a figure of merit of great utility in the development of particle aggregates with the optimal structure for desirable nanosensor response.

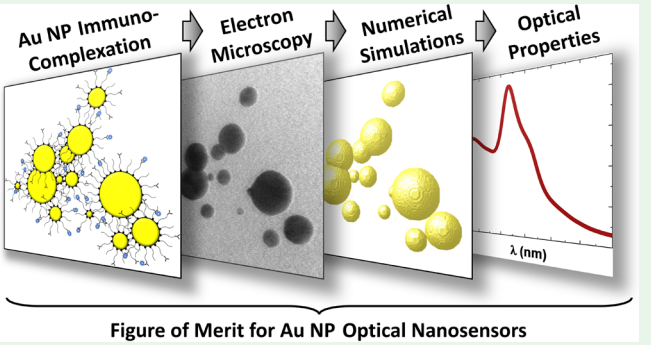

Figure of Merit for Au NP Optical Nanosensors

KEYWORDS: *gold nanoparticles, immunosensors, optical sensors, plasmon absorption, CRP*

INTRODUCTION

Gold nanoparticles (Au NPs) are chemically stable, not toxic, photostable, surface functionalizable in one step with any thiolated ligand,[1,2] and easily synthesizable even at very low cost.[3,4] Most importantly, Au NPs exhibit an intense coloration due to the plasmon resonance band, which is shape-dependent and aggregation-dependent.[5,6] This set of deeply investigated features has been exploited for decades in colorimetric and optical sensing to detect a variety of analytes such as biomolecules, organic compounds, and metal ions.[1,5] The typical Au NP optical sensor is based on the specific molecular recognition between a receptor bound to the particle surface and an antigen to be detected.[1,7−9] The receptor can be an antibody, scFv, nanobody, aptamer, or any other chemical function selective for the analyte.[1,7,8,10−12] When Au NPs are conjugated with antibodies, the binding of the antigen will induce specific particle aggregation by immunocomplexation.[1,5,7,12,13]

While the working principle of Au NP optical sensors is simple and general, there is a list of parameters which influence their response, such as the particle size and shape, interparticle distance, and number and disposition of particles in the aggregate.[14−18] The variety of these parameters has a direct correspondence with the different responses reported so far for this class of detection systems. Indeed, several examples of colorimetric sensors based on Au NPs have been proposed in recent times.[19−21] For instance, a colorimetric serological assay to detect SARS-CoV-2 IgG antibodies was developed by coating Au NPs with epitopes located on the spike and nucleocapsid proteins of the virus.[22] Another example consists in the evolution of the optical properties of Au NPs functionalized with a red blood cell membrane, which has been assessed over time in the presence of the antigen fibrinogen to identify the best timing and spectroscopic features for analytical applications.[23] Aptamer-conjugated Au NPs showed reversible aggregation in the presence of analyte thrombin and external physical stimuli such as ultrasound.[24] In a model albumin assay, a mixture of 20 and 50 nm Au NPs was shown to enhance the signal compared to the single-sized 20 nm Au NP samples and to provide acceptable colloidal stability compared to the single-sized 50 nm Au NPs.[15]

However, the precise correlation between the NP aggregate structure and optical properties still requires a clear identification in most of the nanosensors described in the literature, introducing a gap of uncertainty about design criteria

Received: October 12, 2021
Accepted: December 10, 2021
Published: December 28, 2021

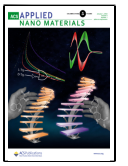

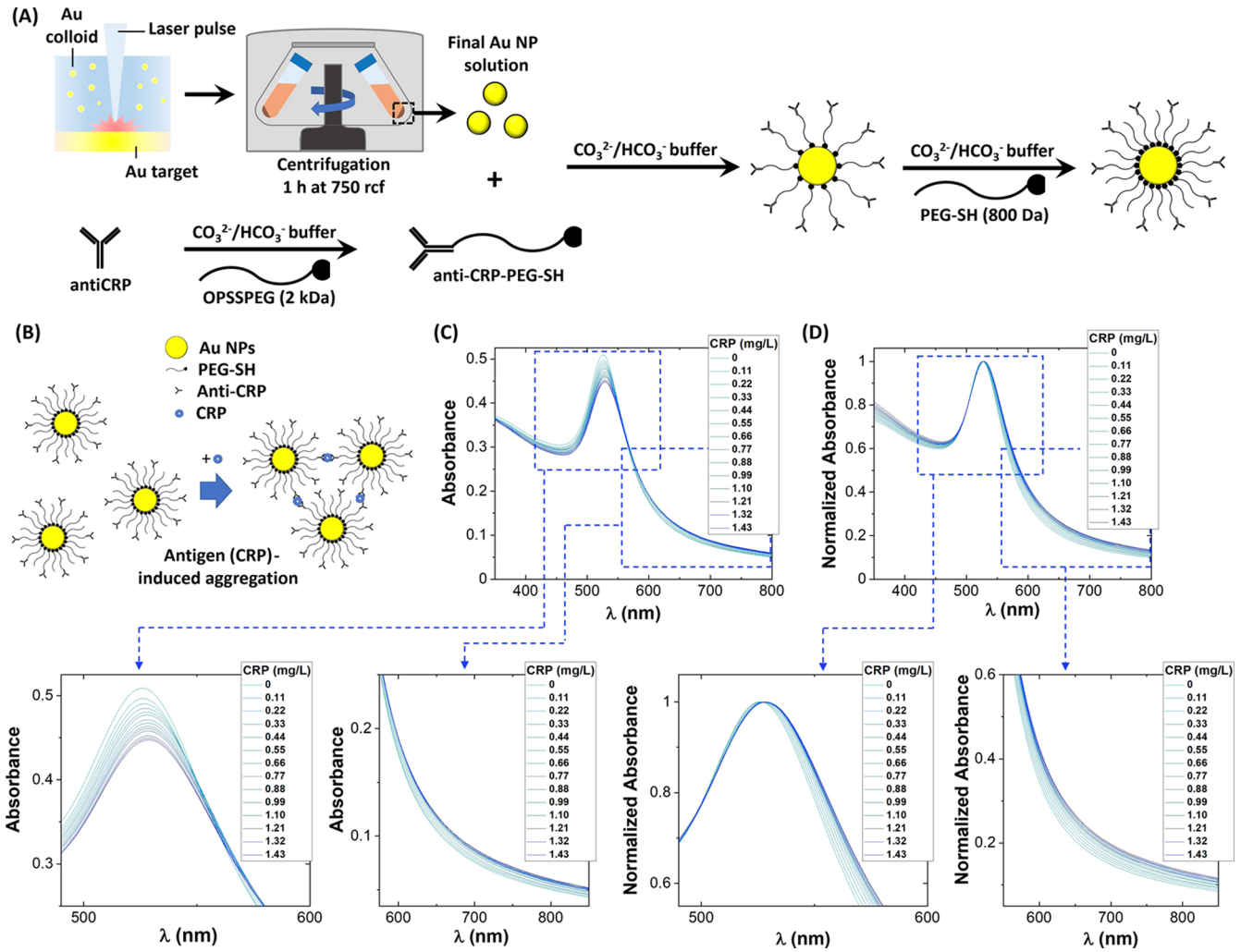

Figure 1. (A) Sketch of the synthetic procedure for immunoconjugated Au NPs. (B) Sketch of the immunocomplex formation in the solution of Au NPs coated with anti-CRP-PEG-SH: the coordination of CRP (antigen) induces Au NP aggregation and consequent changes on the optical properties. (C,D) UV−vis spectra of Au NPs coated with anti-CRP-PEG-SH upon the addition of CRP up to 1.43 mg/L, reported in absolute absorbance (C) and after normalization to the plasmon peak absorbance (D). The magnification of regions affected by the most relevant spectral changes is also reported.

for the bioconjugate and the best practice for the analysis of the optical response. It is thus of utmost importance to elucidate the optical properties of immunocomplexes which can guide the design and development of new Au NP optical sensors for a specific analyte.[14,15] This is especially relevant for nanosensors affected by a limited detection interval, which may block the exploitability for real life application. Typically, a limited detection interval is due to low sensitivity, signal saturation already at a low analyte concentration, or the "hook" effect, namely, the disaggregation of immunocomplexes when the analyte concentration exceeds a threshold defined by the affinity constant of the receptor−antigen couple.[25,26]

Here, we studied the optical properties of an Au NP immunosensor, identifying the spectroscopic features most relevant for analytical purposes and their correlation with the immunocomplex structure by using transmission electron microscopy (TEM) and numerical calculations of the observed plasmonic absorption. To this end, we selected the model immunocomplexation reaction between human C-reactive protein (CRP) and its antibody (anti-CRP), which were immobilized on the Au NP surface. CRP is an important biomarker involved in the organism response to inflammation states, during which its plasma concentration can increase to up to hundreds of milligrams per liter.[27] This feature is routinely used for monitoring a variety of clinical conditions such as cancer and cardiovascular and neurological diseases.[7,27,28] Hence, several assays based on the change of the physical properties of Au NPs functionalized with receptors of CRP have been proposed, including optical sensors.[7,26,29−31]

MATERIALS AND METHODS

Synthesis. The Au NPs were synthesized by laser ablation in liquid (LAL).[4,32] In LAL, the laser pulses at 1064 nm (6 ns, 50 Hz) were focused to 8 J/cm^2 with an f 100 mm lens on a 99.99% pure Au plate dipped in distilled water with 10^{-4} M NaCl. Then, the colloid of Au NPs was centrifuged for 1 h at 50 rcf to discard the heavy fraction and for 1 h at 250 rcf to collect the sediment and discard the supernatant containing the smallest NPs. The resulting Au NP size, assessed by TEM with the ImageJ software on >800 NPs, was 17 nm with a standard deviation of 12 nm and a lognormal size distribution. No other additives or solutes were used for the synthesis of Au NPs, which have a surface free of contaminants and ready for bioconjugation.

The anti-CRP-PEG-SH conjugate was obtained in the following steps:[30]

https://doi.org/10.1021/acsanm.1c03380
ACS Appl. Nano Mater. 2022, 5, 578−586

(i) Antibody concentration in the conjugation buffer. Before performing the conjugation reaction, the anti-CRP [goat antibody to human CRP, immunoglobulin G, affinity purified, MW = 150 kDa and ε(280 nm) = 210,000 M^{-1} cm^{-1}, purchased from IIC at 10 mg/mL—0.066 mM] was concentrated to 10.5 μM in a CO_3^{2-}/HCO_3^- buffer at a pH of 9.2 by exhaustive dialysis. To this purpose, 2 mL of the initial solution of anti-CRP was dispersed in 20 mL of buffer and centrifuged two times in Vivaspin PES 10 kDa concentration membranes for 30 min (3864 rcf, 20 °C) using a MPW351 centrifuge equipped with a swing-out rotor.

(ii) Conjugation. 3000 μL of the 46.2 μM anti-CRP solution (0.13 μmol) and 7500 μL of 36.7 μM OPSSPEG (orthopyridyldisulfide-polyethyleneglycol-*N*-hydroxysuccinimide, 2 kDa, purchased from Creative PEGworks) solution (0.082 mg/mL, 0.26 μmol) in sodium bicarbonate (100 mM, pH 8.5) were mixed in a round-bottom flask and magnetically stirred overnight at 4 °C.

(iii) Purification. The reaction mixture was purified by dialysis within the same buffer (centrifuged two times in Vivaspin PES 10,000 Da with 20 mL of buffer for 20 min). The final solution was used for the next step of Au NP conjugation with the antibody.

The immunoconjugate of Au NPs and anti-CRP-PEG-SH was obtained in the following steps:[30]

(i) Bioconjugation. The Au NP solution (9.9 nM) was mixed with the anti-CRP-PEG-SH solution (41.4 μM) at a volume ratio of 500:9, corresponding to a ratio of anti-CRP/Au NPs of 75. This ratio was selected based on previous binding studies of anti-CRP-PEG-SH on Au NPs, suggesting that the surface of the particles is close to complete coverage at >50 anti-CRP-PEG-SH for each Au NP.[30] A bicarbonate buffer solution was also added at a volume ratio of 192:509 with the previous solutions. A volume ratio close to 2:5 for the buffer and Au NP solution was selected to avoid excessive dilution and accelerate the subsequent washing steps. The solution was incubated for 2 h at 4 °C, namely, in the same reaction bath as that of the previous steps and for a time long enough to achieve the conjugation of the thiolated PEG derivatives on the free surface of laser-generated Au NPs.

(ii) Au NP surface saturation. PEG-SH (8 μM, 800 Da, Sigma-Aldrich) at a volume ratio of 10:701 with the previous solutions (*corresponding* to ca. 20% of the mol of anti-CRP-PEG-SH) was added for the total saturation of the NP surface, and the solution was incubated for an additional 2 h at 4 °C. The 800 Da PEG-SH has lower steric hindrance than anti-CRP-PEG-SH; thus, it can saturate the surface of the Au NPs which may have remained available after coating with the bioconjugate PEG ligand. In this way, stabilization of the Au NPs is maximized against nonspecific adsorption of serum proteins.

(iii) Purification and resuspension in Ca^{2+} buffer. The Eppendorf tubes containing the bioconjugates were centrifuged at 13.2 krpm for 20 min twice to remove the supernatant. The precipitate was diluted in HEPES 20 mM buffer with 1 mM Ca^{2+}, reaching a final concentration of immunoconjugated Au NPs of 2.0 nM.

A sketch of the process for the preparation of immunoconjugated Au NPs is shown in Figure 1A.

Immunocomplexation. To 900 μL of immunoconjugated Au NPs (2 nM), increasing aliquots of a standard CRP solution (CRP calibrator 52.0 mg/L, 455 nM, from AMS, datasheet ref. GD8429_00) were added. The final achieved antigen concentrations (in mg/L) were 0, 0.11, 0.22, 0.33, 0.44, 0.55, 0.66, 0.77, 0.88, 0.99, 1.1, 1.21, 1.32, and 1.43, corresponding to the addition of 0, 2, 4, 6, 8, 10, 12, 14, 16, 18, 20, 22, 24, and 26 μL, respectively, of the standard solution with a high precision calibrated micropipette. The ultraviolet—visible (UV—vis) spectroscopy and other measurements were performed just after the addition, following the results of preliminary experiments where the mixtures have been monitored at different antigen volumes and aging times to confirm that the optical absorption remained constant from a few seconds to tens of minutes after antigen addition. As a control, UV—vis spectroscopy was performed on the same immunoconjugated Au NPs upon the addition of 0, 2, 4, 6, 8, 10, 12, 14, 16, 18, 20, 22, 24, and 26 of a serum protein (bovine serum albumin, BSA, 40,000 mg/L) solution with the same protein concentration of the real serum containing CRP (see Figure S1 in the Supporting Information), and no effects were observed due to BSA nonspecific interaction, in agreement with our previous study.[30]

The UV—vis spectra were analyzed after the correction for the dilution factor given by $(V_{add} + V_0)/V_0$, where V_0 is the initial volume and V_{add} is the volume of each antigen addition.

Characterization. UV—vis spectroscopy was performed in 0.2 cm optical path quartz cuvettes using a JASCO V770 spectrophotometer. Dynamic light scattering (DLS) analysis was performed using a Malvern Zetasizer Nano ZS in ZEN0040 cells. TEM was performed on a FEI Tecnai G2 12 instrument operating at 100 kV and equipped with a Veleta (Olympus Soft Imaging System) digital camera. Following the procedure described in refs 33 and 34, before the deposition, the Au NP samples were mixed in a 1:10 vol/vol ratio with a 10 mg/mL solution of polyvinyl alcohol (PVA, 87—89% hydrolyzed, 18 kDa) in deionized water. Then, one drop of the mixture was cast on a 400-mesh carbon-coated copper grid, with the excess liquid removed by capillarity with laboratory paper and the liquid remaining on the grid left to dry in air at room temperature. Note that the NP solutions were diluted 1/10 vol/vol with the PVA solution also to avoid accidental agglomeration of particles during solvent drying. No effects on the Au NP optical absorption spectra were observed upon the addition of the aqueous PVA solution (as shown in Figure S2 in the Supporting Information).

Numerical Calculations. The extinction cross-section (σ_{ext}) of the Au NP aggregates was evaluated through numerical calculations based on discrete dipole approximation (DDA) using the DDSCAT code.[35] The targets representing the different aggregates of Au NPs were created ad hoc with the same structure (NP size and geometric position) as that observed from the TEM pictures.

The number of dipoles (N) was set between 10^4 and 10^5 to minimize the computational errors on the absolute value of the extinction cross-section and to allow reliable comparison of calculated optical properties for the different targets.[35−37] This guaranteed an interdipole spacing at least 0.08 times smaller than the NP size and at least 0.005 times smaller than the incident wavelength in the 325—900 nm range. In effect, for metal particles in the 2—200 nm size range, an error smaller than 10% is achieved using an interdipole spacing much smaller than the wavelength of interest.[35−37] Results were further checked for convergence for several targets by increasing the number of dipoles, which allowed us to confirm the accuracy of results well below 5%.

All the calculated σ_{ext} values resulted from the arithmetic average over two orthogonal polarization directions and 27 sets of Euler angles of rotation of the target with respect to the incident plane wave (i.e., a total of 54 different orientations for each σ_{ext}) to simulate the dispersion of immunocomplexes with a random orientation in the liquid solution.

The effect of the water solvent was accounted for by setting the refractive index of the nonabsorbing matrix to 1.334. The complex dielectric constant of Au was obtained from ref 38 and corrected for the intrinsic size effects according to what was described in refs 5 39, and 40.

RESULTS

In this study, the anti-CRP unit was conjugated by an amide chemical bond with a 2000 Da polyethylene glycol spacer with a thiol group on the opposite end (PEG-SH). In this way, anti-CRP retains the necessary orientational freedom for binding the antigen, even after the immobilization of the anti-CRP-PEG-SH unit on the surface of Au NPs by the formation of the

https://doi.org/10.1021/acsanm.1c03380
ACS Appl. Nano Mater. 2022, 5, 578—586

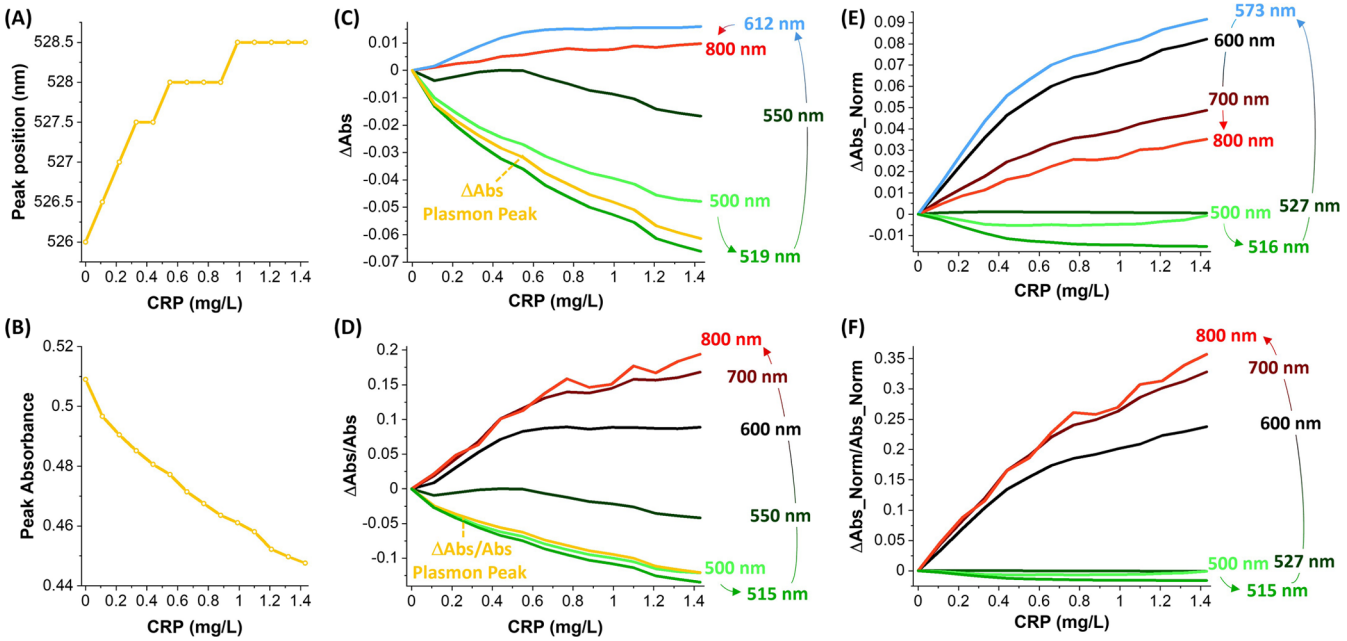

Figure 2. (A) Plasmon peak position (in nm) vs CRP concentration. (B) Plasmon peak absolute absorbance vs CRP concentration. (C) Change in absolute absorbance (ΔAbs) vs CRP concentration at different wavelengths from 500 (light-green line) to 800 nm (red line). The lowest and highest curves are found at, respectively, 519 nm (green line) and 612 nm (blue line). The ΔAbs at the plasmon peak is reported as a yellow line. (D) Relative change of absolute absorbance (ΔAbs/Abs) vs CRP concentration at different wavelengths from 500 (light-green line) to 800 nm (red line). The lowest and highest curves are found at, respectively, 515 nm (green line) and 800 nm. The ΔAbs at the plasmon peak is reported as a yellow line. (E) Change in normalized absorbance (ΔAbs_Norm) vs CRP concentration at different wavelengths from 500 (light-green line) to 800 nm (red line). The lowest and highest curves are found at, respectively, 516 nm (green line) and 573 nm (blue line). (F) Relative change of normalized absorbance (ΔAbs_Norm/Abs_Norm) vs CRP concentration at different wavelengths from 500 (light-green line) to 800 nm (red line). The lowest and highest curves are found at, respectively, 515 nm (green line) and 800 nm. The trend in (C−D−E−F) is described by the arrows.

sulfur−gold chemical bond (Figure 1A). The surface of Au NPs is finally saturated with a shorter PEG-SH (800 Da) to avoid any nonspecific interaction between the particle surface and the constituents of serum in the human CRP samples. Hence, the colloid of Au NPs conjugated with anti-CRP-PEG-SH can form immunocomplexes after the addition of real samples containing the antigen (Figure 1B), as previously demonstrated by immunofluorimetric assays.[30] The UV−vis spectra of the sensor solution upon the addition of increasing amounts of CRP (Figure 1C) show a change in the surface plasmon resonance, as indicated by the decrease of plasmon peak absorption in the proximity of 520 nm, which is associated with the formation of immunocomplexes. The other spectral changes are better appreciable from the UV−vis spectra normalized on the plasmon peak (Figure 1D), such as the red shift of the plasmon band and the increase in the optical density in the 550−800 nm range.

From this set of spectral changes, the quantitative detection of the analyte concentration can be performed using as endpoints the plasmon peak position, the plasmon peak absorbance, or the change in absorbance at a convenient wavelength. The plasmon peak position (i.e., the wavelength at which the maximum of the plasmon absorption occurs, according to the spectrum recorded by the UV−vis spectrometer) increases with the CRP concentration (Figure 2A), but the typical resolution of UV−vis spectrophotometers is unfit for the continuous monitoring of this parameter. For instance, under our experimental conditions, the spectrometer registered the absorbance at an interval of 0.5 nm, which is less than the resolution required to monitor the red shift of the plasmon peak in the experiment, resulting in a plot of the peak position changing discontinuously with a step of 0.5 nm. Although this problem may be resolved by increasing the spectral resolution or by a Lorentzian fit of the absorption peak, these operations are time-consuming and suggest resorting to absorbance as a parameter that varies continuously in the interval of interest. Indeed, the UV−vis spectrometers are built to offer the best performances for this type of measurement. The absorbance at the plasmon peak decreases continuously with the CRP concentration (Figure 2B). However, the spectral position of the plasmon peak changes when the analyte concentration is increased. Instead, a fixed spectral position would be more convenient for monitoring the immunocomplexation process in a real nanosensor. Usually, this spectral position is arbitrarily identified in the red or near-infrared regions. In this case, the absolute change of absorbance (ΔAbs) at all wavelengths between 500 and 800 nm was plotted (Figure 2C) to identify the best spectral position for quantitative assessment in our experimental conditions. The plot of Figure 2C indicated a decreasing trend for wavelengths in the proximity of the plasmon peak, as anticipated in Figure 1B, and an increasing trend in the red and infrared regions. In more detail, a negative ΔAbs is observed at wavelengths from 500 to 550 nm, with the largest values measured at 519 nm. At this wavelength, the change in absorbance is even larger than that at the plasmon peak, thus indicating a better sensitivity for the nanosensor, intended as the change in the response versus the change in the analyte concentration. At 550 nm, the ΔAbs becomes positive for a small CRP concentration, with the largest positive value

https://doi.org/10.1021/acsanm.1c03380
ACS Appl. Nano Mater. 2022, 5, 578−586

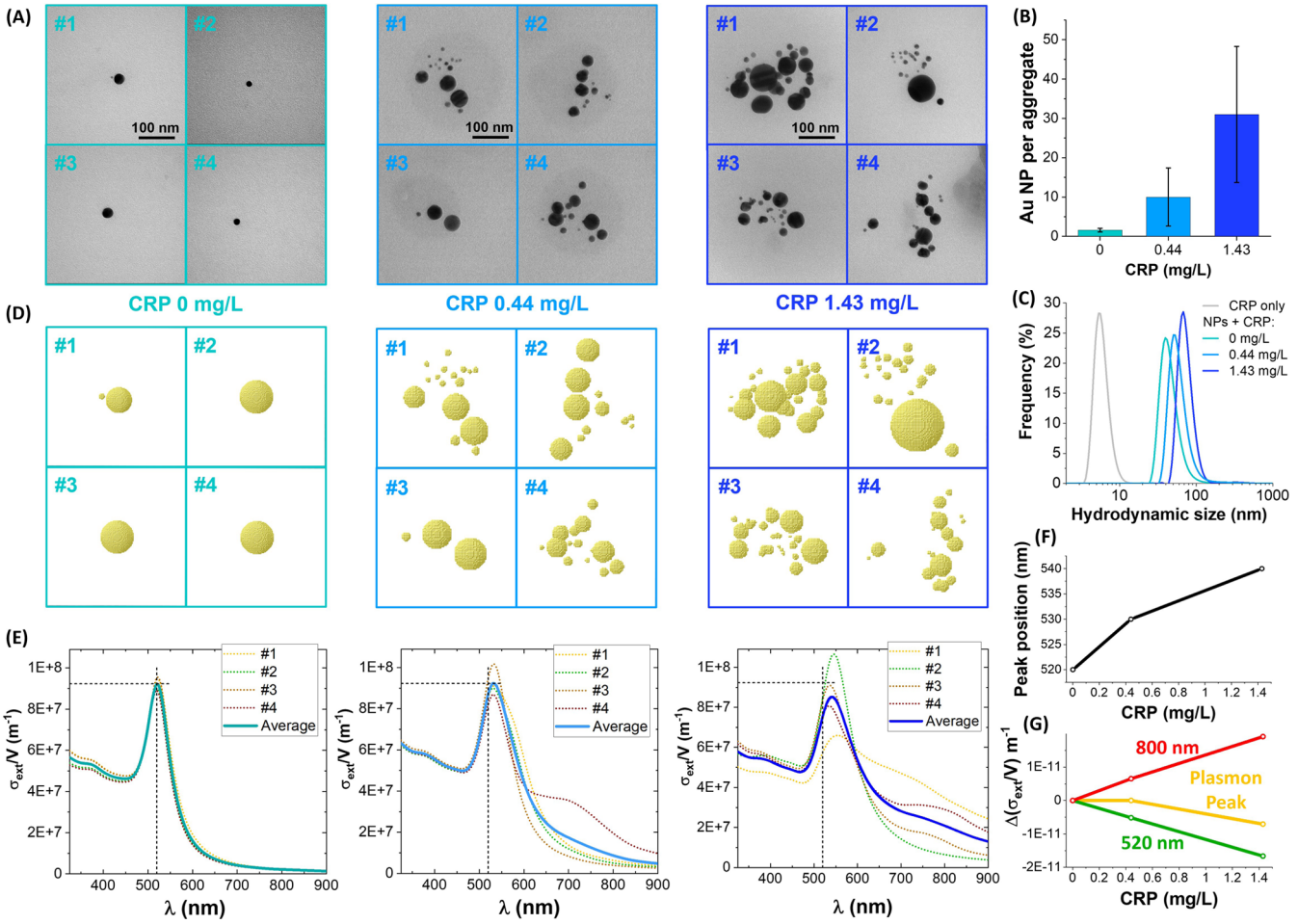

Figure 3. (A) Representative TEM images of Au NP aggregates of the three samples at 0, 0.44, and 1.43 mg/L CRP. PVA was added before the deposition to preserve the aggregate structure and interparticle distance and avoid additional agglomeration during solvent evaporation. (B) Average number of Au NPs in aggregates observed by TEM. (C) DLS analysis of the three Au NP samples and of free CRP. (D) Targets used for DDA calculations of the corresponding extinction cross-sections. (E) Extinction cross-section normalized to the total volume of Au NPs (σ_{ext}/V) for the aggregates showed in (A), reported as dotted lines for the single aggregate and as a continuous line for the resulting average. The position and σ_{ext}/V of the plasmon peak for the sample with 0 mg/L CRP are indicated by the black dashed lines. (F,G) Calculated peak position (F) and extinction change $\Delta\sigma_{ext}/V$ (G) for the three samples.

measured at 612 nm. The trend remains positive until 800 nm, but it should be noted that in the red spectral region, the nanosensor response saturates (the curve becomes flat) already at 0.5−0.6 mg/L of CRP.

Given the higher optical density in the proximity of the plasmon resonance, the plot of the relative absolute absorbance ΔAbs/Abs is also meaningful to stress the relative increment of optical density over the whole 500−800 nm spectral range (Figure 2D). Here, it is shown that the relative change at 500−520 nm is comparable, with a minimum at 515 nm. The maximum is found at 800 nm, but the low absolute intensity also implies the largest influence from the experimental error.

The normalization to the plasmon peak is useful for evidencing the spectral differences due to immunocomplex formation; hence, the change in absorbance in the normalized UV−vis spectra (ΔAbs_Norm) has been considered at all wavelengths between 500 and 800 nm (Figure 2E). The general scenario is similar to that of ΔAbs, with a decrease in response from 500 to 516 nm, a trade-off at 527 nm, and an increase up to a maximum at 573 nm, after which the response remains positive but of lower intensity until 800 nm. The largest response is found at 573 nm and is due to an increase in ΔAbs_Norm. When the relative normalized absorbance (ΔAbs_Norm/Abs_Norm) is considered, the general trend shows a limited decrease from 500 to 515 nm and a trade-off at 537 nm where the response is positive, after which it continuously grows until 800 nm, where the noise due to the experimental error becomes comparable to the signal change due to the low absolute absorbance.

It is worth stressing that in all the best cases of Figure 2, the nanosensor did not exhibit the hook effect, even at the maximum CRP concentration, which corresponds to acute inflammation conditions.[7,27,28] The behavior of the nanosensor was also tested at concentrations higher than those typical of the acute inflammation conditions, that is, up to 3.3 mg/L CRP, without observing a recovery of the spectral changes due to the hook effect.

Then, we investigated the structure of immunocomplexes at three relevant stages of the process over the whole range of the experiment, namely, without the analyte, at intermediate amounts of the analyte (0.44 mg/L CRP), and at the upper analyte limit of this experiment (1.43 mg/L CRP). For TEM, the Au NP solutions were mixed with PVA (see the Materials and Methods section and the Supporting Information for

https://doi.org/10.1021/acsanm.1c03380
ACS Appl. Nano Mater. 2022, 5, 578−586

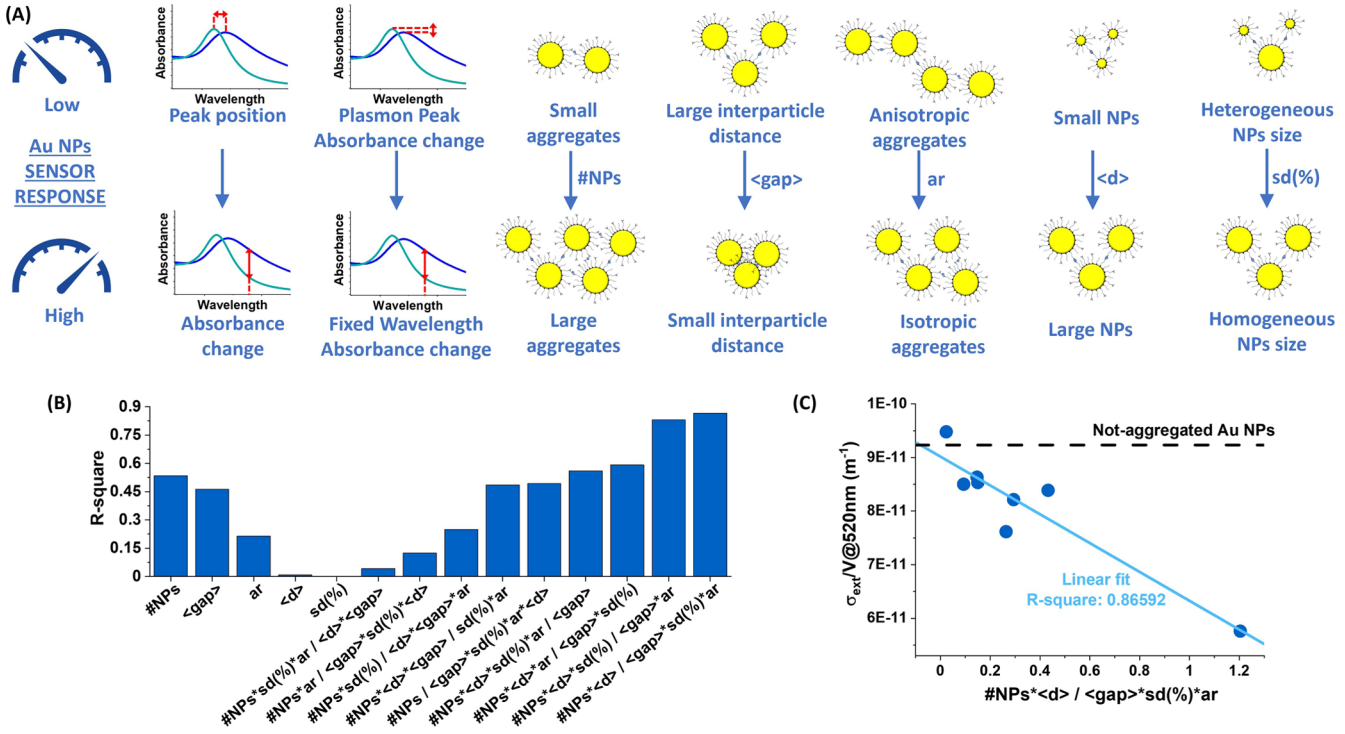

Figure 4. (A) Sketch of the panel of parameters guiding the design of efficient optical sensors based on Au NPs. (B) *R*-square of the linear regression applied to the plot of σ_{ext}/V (at 520 nm) for the eight Au NP aggregates reported in Figure 3 as a function of the parameter or combination of parameters indicated in the histogram. (C) Plot of the σ_{ext}/V (at 520 nm) for the eight Au NP aggregates vs the FOM of eq 1, which has the highest *R*-square among those tested (circles). The corresponding linear regression (continuous line) and the σ_{ext}/V (at 520 nm) for isolated Au NPs (dashed line, according to the calculation in Figure 3E) are also reported.

details) before drop-casting on the TEM grid, following a well-established procedure that preserves the aggregate structure and avoids additional agglomeration during the liquid evaporation on the grid.[33,34] TEM images (Figure 3A and Figure S3 in the Supporting Information) clearly show the evolution of Au NPs from the fully dispersed state (0 mg/L CRP) to the immunocomplexed state (0.44 and 1.43 mg/L CRP). This is quantifiable with the statistics of the number of Au NPs per aggregate in the three samples (Figure 3B), which results in 1.6 ± 0.5 at 0 mg/L CRP, 10 ± 7 at 0.44 mg/L CRP, and 31 ± 17 at 1.43 mg/L CRP. DLS (Figure 3C) confirms this trend, with an average hydrodynamic size of 47 ± 22 nm at 0 mg/L CRP, 62 ± 29 nm at 0.44 mg/L CRP, and 73 ± 16 nm at 1.43 mg/L CRP, while for the CRP alone, the measured average size is 5.9 ± 1.3 nm. The discrepancy between the Au NP size measured using TEM and DLS may be due to the role of Brownian motion in the colloidal solution, which has been suggested to depend on the shape, size, composition, and surface chemistry of particles, thereby contributing in various ways to particle−solvent interactions, especially in the case of anisotropic or fractal structures.[41] *Z*-potential analysis of the three samples (Figure S4 in the Supporting Information) did not evidence any remarkable difference or trend versus the CRP concentration, thus confirming that Au NP aggregation occurs for antigen−antibody interaction and not for a change in the colloidal stability of the immunoconjugated Au NPs.

Noticeably, TEM images of Figure 3A show that Au NPs in the immunocomplexes are not densely packed yet are arranged at distances of several nanometers, often comparable to the NP size, in accordance with the presence of the spacing due to CRP, anti-CRP, and the PEG spacer between anti-CRP and the gold surface.[42−44] The measured thickness of CRP bound to anti-CRP is 2 nm, despite the fact that the longitudinal size of the CRP pentamer is of the order of 10 nm, in agreement with the overall hydrodynamic size of 5.9 ± 1.3 nm measured using DLS.[44] The thickness of an anti-CRP layer is also of the order of 2 nm according to atomic force microscopy measurements.[44] Besides, the chain of 2000 Da PEG can extend up to ∼10 nm in its brush conformation.[42,43] Therefore, the spacing between Au NPs in TEM images is compatible with their surface bioconjugation and antigen-induced aggregation after the inclusion in the dried PVA matrix.

The interparticle distance has crucial importance for the optical properties of Au NP aggregates, but the complex fractal structure and the variety of interparticle distances do not allow for an easy prediction of the resulting optical properties of the immunocomplexes just from TEM images. Thus, the DDA method[36,40,45] was used to accurately reproduce the position and shape of Au NPs in the aggregates (Figure 3D) and calculate the corresponding extinction cross-section (σ_{ext}, see the Materials and Methods section and the Supporting Information for details). It should be noted that the TEM images provide a 2D projection of 3D objects embedded in the polymeric matrix after water evaporation and that the interparticle distance in the actual solution may be different (likely larger) than that in the dried PVA matrix; hence, the DDA simulations are just a first approximation of the expected extinction profiles for the corresponding tridimensional immunocomplexes in the colloidal solution. For instance, it should be considered that 2D targets tend to emphasize the aspect ratio and the consequent effects on the extinction profiles compared to the 3D structure yet retain the main spectral features and interparticle distances and provide

https://doi.org/10.1021/acsanm.1c03380
ACS Appl. Nano Mater. 2022, 5, 578−586

qualitative trends for the optical properties of immunoaggregates.

As shown in Figure 3E, the orientational average of the σ_{ext} calculated with the DDA method was divided for the volume (V) of each object to allow for the direct comparison of the optical properties independent of the number and size of Au NPs considered. At 0 mg/L CRP, the spectral profiles of the four targets (dotted lines) are very similar and nearly overlap with their average (red line), with a plasmon peak centered at 520 nm with a σ_{ext}/V of 9.23×10^{-11} m^{-1} (highlighted by the dashed black lines in the plot). At 0.44 mg/L CRP, the extinction shows a dependence on the aggregate type (dotted lines), with a difference between complexes with an elongated structure such as #2 and #3 and the complexes such as #1 and #4 having a more isotropic ramification (higher fractal number). The average of the calculated σ_{ext}/V profiles exhibits the red shift of the plasmon peak (at 530 nm) and the increase in the optical density in the red region. This is quite appreciable by the comparison of the average σ_{ext}/V of the four aggregates (black line) with the position for the 0 mg/L CRP sample (dashed black lines). The plasmon peak maximum of the calculated σ_{ext}/V resulted to be 9.23×10^{-11} m^{-1}.

The trend further persists in the calculations for the 1.43 mg/L CRP sample, with the average σ_{ext}/V of 8.52×10^{-11} m^{-1} and peaked at 540 nm. Although remarkable spectral differences are observed among the four aggregates (see #1 and #3 vs #2 and #4), all of them show a red shift and the increase in absorbance in the red and near-infrared regions.

Overall, the numerical calculations succeeded in reproducing the experimental trends of Figure 2 with increasing NP aggregation, namely, the red shift of the plasmon peak (Figure 3F), the decrease in the optical density at wavelengths shorter than the plasmon peak of isolated Au NPs, and the concomitant increase of light extinction in the red and near-infrared regions (Figure 3G). The plots of Figure 3F,G also support the experimental data in indicating that the sensitivity is larger and more reliable at 520 nm or 800 nm than that at the plasmon peak. This is an indication that the approach based on the TEM analysis and DDA calculations was able to reproduce qualitatively the optical behavior of Au NP immunoaggregates in the colloidal solution. On the other hand, it is worth noticing that the studies which addressed the optical behavior of immunoaggregated Au NPs in conditions as close as possible to those in the colloidal solution are really limited in number,[1,5] despite the technological relevance of these systems.

DISCUSSION

Taken together, the experiment and calculations indicate that the change in optical properties depends crucially on the selected wavelength, with the optimum in terms of ΔAbs and signal-to-noise ratio expected in the proximity of the plasmon peak. The change in absorbance is more precise and has better linearity than the spectral shift of the plasmon peak (Figure 4A).

Concerning the structure of the aggregates, calculations show that the spectral modifications increase with the number of Au NPs in the aggregate. Besides, the PEG spacer between the receptor and the Au NP surface has the effect of keeping an interparticle distance of several nanometers in the immunocomplexes,[42,43] with a consequent effect on the resulting optical properties. That the extinction cross-section undergoes a higher red shift and broadening when the interparticle distance is lower is suggested, for instance, by the comparison of the calculated extinction profile for aggregates #1 (interparticle distance generally lower than the NP size) and #3 (interparticle distance generally comparable to the NP size) in the 1.43 mg/L CRP sample of Figure 3.

Another observation is that elongated aggregates have a lower red shift and plasmon peak broadening than isotropic aggregates (for instance, aggregates #2 and #3 with respect to aggregates #1 and #4 in the 0.44 mg/L CRP sample of Figure 3). This may be related to the fact that the orientational average of elongated aggregates considers several orientations where the plasmon band is similar to that of isolated particles (incident electric field along the main axis of the aggregate), which is not the case for isotropic aggregates with different optical properties along all the directions.[5,46] Overall, one can infer that the number of receptors and their orientational degree of freedom on the Au NP surface should be maximized for optimal nanosensor response. The role of the aggregate aspect ratio also becomes very relevant in other classes of Au NP nanosensors, such as those based on fluorescence dequenching, where the orientation of anisotropic aggregates with respect to polarized light and fluorophores is crucial for an optimal response.[47,48]

The average NP size may have a contribution in explaining the larger change in σ_{ext}/V (at 520 nm) for aggregate #4 than that for aggregate #1 in the 0.44 mg/L CRP sample of Figure 3, as well as for aggregate #1 than that for aggregate #4 in the 1.43 mg/L CRP sample of Figure 3. The calculations also indicate a larger red shift and broadening of the plasmon peak when the NPs of the immunocomplex are of comparable size, instead of being constituted of small particles and a single larger NP, as shown by aggregate #2 of the 1.43 mg/L CRP sample of Figure 3.

In summary, from the numerical calculations, it is possible to identify five parameters of Au NP aggregates with a possible effect on their optical properties (Figure 4A): the number of Au NPs in the aggregate (#NPs), the average of the minimum interparticle distance among next-neighbor NPs (⟨gap⟩), the aspect ratio of the aggregate (i.e., the ratio of its length to its width, ar), the average size of the NPs in the aggregate (⟨d⟩), and the corresponding standard deviation [expressed in percentage, sd(%)]. As a first approximation, linear regression can be used to verify the existence of a correlation between the calculated σ_{ext}/V (at 520 nm) and each of the five parameters for the Au NP aggregates of Figure 3. The R-square of the linear regressions, reported in Figure 4B, suggests a possible correlation with #NPs and ⟨gap⟩. To further verify a cross-correlation between the five parameters, according to the observations reported above, a combinatorial linear regression approach was applied to a figure of merit (FOM) depending on #NPs, ⟨gap⟩, ar, ⟨d⟩, and sd(%). In all combinations, the proportionality of the σ_{ext}/V (at 520 nm) with the #NP was the only constraint, while the correlation with other parameters has been checked considering the R-square of the linear regression. The results of Figure 4B−C show that the best R-square is found for the adimensional FOM

$$\mathrm{FOM} = \frac{\#\mathrm{NPs}\ \langle d\rangle}{\langle gap\rangle\ \mathrm{ar}\ \mathrm{sd}(\%)} \quad (1)$$

which is in agreement with all the above observations extracted from the calculated extinction cross-sections. Thus, eq 1 can be

https://doi.org/10.1021/acsanm.1c03380
ACS Appl. Nano Mater. 2022, 5, 578−586

considered a possible FOM for the design of optical sensors based on Au NP aggregation. However, it is worth noticing that this FOM is extracted from numerical calculations for 2D aggregates of spherical Au NPs; thus, further validation by experimental verification on single aggregates, also with nonspherical particles such as nanorods or nanostars, would be required in the future.[49]

CONCLUSIONS

In summary, the optical properties of a model nanosensor based on the immunocomplexation of anti-CRP-PEG-SH-coated Au NPs in the presence of CRP were studied. The aggregation of NPs is associated with a change in the plasmon peak position and optical density in the 500−800 nm range, with optimal effects in terms of sensitivity and the signal-to-noise ratio depending on the observation wavelength, which is the first relevant parameter for optical sensing. The immunocomplexes were observed by TEM after freezing their structure in a polymeric matrix to verify the relation between the number of Au NPs in the aggregate and the observed optical properties. Numerical simulations for representative immunocomplexes supported and explained the experimental results, in addition to identifying the interparticle distance, size homogeneity, aggregate isotropy, and number of NPs as key parameters for optimal nanosensor response. These results provide a panel of parameters that have been collected in an FOM useful for designing efficient optical sensors based on Au NPs conjugated with any type of receptors for the desired analyte.

ASSOCIATED CONTENT

Supporting Information

The Supporting Information is available free of charge at https://pubs.acs.org/doi/10.1021/acsanm.1c03380.

UV−vis spectra of immunoconjugated Au NPs upon the addition of BSA solutions; UV−vis spectra of Au NPs before and after mixing with a PVA solution; TEM images of the three Au NP samples at 0, 0.44, and 1.43 mg/L CRP; and Z-potential of the three Au NP samples at 0, 0.44, and 1.43 mg/L CRP (PDF)

AUTHOR INFORMATION

Corresponding Author

Vincenzo Amendola − *Department of Chemical Sciences, University of Padova, 35131 Padova, Italy;* orcid.org/0000-0002-9937-7005; Email: vincenzo.amendola@unipd.it

Author

Carlo Bravin − *Department of Chemical Sciences, University of Padova, 35131 Padova, Italy;* orcid.org/0000-0001-6291-3938

Complete contact information is available at: https://pubs.acs.org/10.1021/acsanm.1c03380

Notes

The authors declare no competing financial interest.

ACKNOWLEDGMENTS

This research was funded by the University of Padova P-DiSC project "DYNAMO" and by Alifax S.p.a. (Italy).

REFERENCES

(1) Saha, K.; Agasti, S. S.; Kim, C.; Li, X.; Rotello, V. M. Gold Nanoparticles in Chemical and Biological Sensing. *Chem. Rev.* **2012**, *112*, 2739−2779.
(2) Daniel, M.-C.; Astruc, D. Gold Nanoparticles: Assembly, Supramolecular Chemistry, Quantum-Size-Related Properties, and Applications toward Biology, Catalysis, and Nanotechnology. *Chem. Rev.* **2004**, *104*, 293−346.
(3) Jendrzej, S.; Gökce, B.; Epple, M.; Barcikowski, S. How Size Determines the Value of Gold: Economic Aspects of Wet Chemical and Laser-Based Metal Colloid Synthesis. *ChemPhysChem* **2017**, *18*, 1012−1019.
(4) Crivellaro, S.; Guadagnini, A.; Arboleda, D. M.; Schinca, D.; Amendola, V. A System for the Synthesis of Nanoparticles by Laser Ablation in Liquid That Is Remotely Controlled with PC or Smartphone. *Rev. Sci. Instrum.* **2019**, *90*, 033902.
(5) Amendola, V.; Pilot, R.; Frasconi, M.; Maragò, O. M.; Iatì, M. A. Surface Plasmon Resonance in Gold Nanoparticles: A Review. *J. Phys. Condens. Matter* **2017**, *29*, 203002.
(6) Cacciola, A.; Iatì, M. A.; Saija, R.; Borghese, F.; Denti, P.; Maragò, O. M.; Gucciardi, P. G. Spectral Shift between the Near-Field and Far-Field Optoplasmonic Response in Gold Nanospheres, Nanoshells, Homo- and Hetero-Dimers. *J. Quant. Spectrosc. Radiat. Transfer* **2017**, *195*, 97−106.
(7) António, M.; Nogueira, J.; Vitorino, R.; Daniel-da-silva, A. L. Functionalized Gold Nanoparticles for the Detection of C-Reactive Protein. *Nanomaterials* **2018**, *8*, 200.
(8) Zhang, S.; Geryak, R.; Geldmeier, J.; Kim, S.; Tsukruk, V. V. Synthesis, Assembly, and Applications of Hybrid Nanostructures for Biosensing. *Chem. Rev.* **2017**, *117*, 12942−13038.
(9) Park, J.; Lee, S.; Choi, J.; Choi, I. Extra- and Intracellular Monitoring of TGF-β Using Single Immunoplasmonic Nanoprobes. *ACS Sensors* **2021**, *6*, 1823−1830.
(10) Dekhili, R.; Cherni, K.; Liu, H.; Li, X.; Djaker, N.; Spadavecchia, J. Aptamer-Gold(III) Complex Nanoparticles: A New Way to Detect Cu, Zn SOD Glycoprotein. *ACS Omega* **2020**, *5*, 13851−13859.
(11) Chen, X.; Lisi, F.; Bakthavathsalam, P.; Longatte, G.; Hoque, S.; Tilley, R. D.; Gooding, J. J. Impact of the Coverage of Aptamers on a Nanoparticle on the Binding Equilibrium and Kinetics between Aptamer and Protein. *ACS Sensors* **2020**, *6*, 538−545.
(12) Zeiri, O. Metallic-Nanoparticle-Based Sensing: Utilization of Mixed-Ligand Monolayers. *ACS Sensors* **2020**, *5*, 3806−3820.
(13) Zhang, F.; Huang, P.-J. J.; Liu, J. Sensing Adenosine and ATP by Aptamers and Gold Nanoparticles: Opposite Trends of Color Change from Domination of Target Adsorption Instead of Aptamer Binding. *ACS Sensors* **2020**, *5*, 2885−2893.
(14) Chatterjee, H.; Bardhan, D.; Pal, S. K.; Yanase, K.; Ghosh, S. K. Plasmonic Sensing: Connecting the Dots. *J. Phys. Chem. Lett.* **2021**, *12*, 4697−4705.
(15) Chotithammakul, S.; Cortie, M. B.; Pissuwan, D. Comparison of Single- and Mixed-Sized Gold Nanoparticles on Lateral Flow Assay for Albumin Detection. *Biosensors* **2021**, *11*, 209.
(16) Khlebtsov, B. N.; Tumskiy, R. S.; Burov, A. M.; Pylaev, T. E.; Khlebtsov, N. G. Quantifying the Numbers of Gold Nanoparticles in the Test Zone of Lateral Flow Immunoassay Strips. *ACS Appl. Nano Mater.* **2019**, *2*, 5020−5028.
(17) Caselli, L.; Ridolfi, A.; Cardellini, J.; Sharpnack, L.; Paolini, L.; Brucale, M.; Valle, F.; Montis, C.; Bergese, P.; Berti, D. A Plasmon-Based Nanoruler to Probe the Mechanical Properties of Synthetic and Biogenic Nanosized Lipid Vesicles. *Nanoscale Horiz.* **2021**, *6*, 543−550.
(18) Goyal, G.; Ammanath, G.; Palaniappan, A.; Liedberg, B. Stoichiometric Tuning of PNA Probes to Au0.8Ag0.2 Alloy Nanoparticles for Visual Detection of Nucleic Acids in Plasma. *ACS Sensors* **2020**, *5*, 2476−2485.
(19) Ventura, B. D.; Cennamo, M.; Minopoli, A.; Campanile, R.; Censi, S. B.; Terracciano, D.; Portella, G.; Velotta, R. Colorimetric

Test for Fast Detection of SARS-CoV-2 in Nasal and Throat Swabs. *ACS Sensors* **2020**, *5*, 3043−3048.
(20) Jiang, Y.; Hu, M.; Liu, A.-A.; Lin, Y.; Liu, L.; Yu, B.; Zhou, X.; Pang, D.-W. Detection of SARS-CoV-2 by CRISPR/Cas12a-Enhanced Colorimetry. *ACS Sensors* **2021**, *6*, 1086−1093.
(21) Ma, L.; Peng, L.; Yin, L.; Liu, G.; Man, S. CRISPR-Cas12a-Powered Dual-Mode Biosensor for Ultrasensitive and Cross-Validating Detection of Pathogenic Bacteria. *ACS Sensors* **2021**, *6*, 2920−2927.
(22) Lew, T. T. S.; Aung, K. M. M.; Ow, S. Y.; Amrun, S. N.; Sutarlie, L.; Ng, L. F. P.; Su, X. Epitope-Functionalized Gold Nanoparticles for Rapid and Selective Detection of SARS-CoV-2 IgG Antibodies. *ACS Nano* **2021**, *15*, 12286−12297.
(23) Kim, I.; Lee, D.; Lee, S. W.; Lee, J. H.; Lee, G.; Yoon, D. S. Coagulation-Inspired Direct Fibrinogen Assay Using Plasmonic Nanoparticles Functionalized with Red Blood Cell Membranes. *ACS Nano* **2021**, *15*, 6386−6394.
(24) Zhao, P.; Huo, S.; Fan, J.; Chen, J.; Kiessling, F.; Boersma, A. J.; Göstl, R.; Herrmann, A. Activation of the Catalytic Activity of Thrombin for Fibrin Formation by Ultrasound. *Angew. Chem., Int. Ed.* **2021**, *60*, 14707−14714.
(25) Schiettecatte, J.; Anckaert, E.; Smitz, J. *Interferences in Immunoassays*; IntechOpen: Rijeka, 2012.
(26) Byun, J.-Y.; Shin, Y.-B.; Kim, D.-M.; Kim, M.-G. A Colorimetric Homogeneous Immunoassay System for the C-Reactive Protein. *Analyst* **2013**, *138*, 1538−1543.
(27) Black, S.; Kushner, I.; Samols, D. C-Reactive Protein. *J. Biol. Chem.* **2004**, *279*, 48487−48490.
(28) Sproston, N. R.; Ashworth, J. J. Role of C-Reactive Protein at Sites of Inflammation and Infection. *Front. Immunol.* **2018**, *9*, 754.
(29) António, M.; Ferreira, R.; Vitorino, R.; Daniel-da-Silva, A. L. A Simple Aptamer-Based Colorimetric Assay for Rapid Detection of C-Reactive Protein Using Gold Nanoparticles. *Talanta* **2020**, *214*, 120868.
(30) Bravin, C.; Amendola, V. Wide Range Detection of C-Reactive Protein with a Homogeneous Immunofluorimetric Assay Based on Cooperative Fluorescence Quenching Assisted by Gold Nanoparticles. *Biosens. Bioelectron.* **2020**, *169*, 112591.
(31) Iwasaki, Y.; Kimura, T.; Orisaka, M.; Kawasaki, H.; Goda, T.; Yusa, S.-i. Label-Free Detection of C-Reactive Protein Using Highly Dispersible Gold Nanoparticles Synthesized by Reducible Biomimetic Block Copolymers. *Chem. Commun.* **2014**, *50*, 5656−5658.
(32) Amendola, V.; Amans, D.; Ishikawa, Y.; Koshizaki, N.; Scirè, S.; Compagnini, G.; Reichenberger, S.; Barcikowski, S. Room-Temperature Laser Synthesis in Liquid of Oxide, Metal-Oxide Core-Shells, and Doped Oxide Nanoparticles. *Chem.—Eur. J.* **2020**, *26*, 9206−9242.
(33) Amendola, V. A General Technique to Investigate the Aggregation of Nanoparticles by Transmission Electron Microscopy. *J. Nanosci. Nanotechnol.* **2014**, *15*, 3545−3551.
(34) Amendola, V. Correlation of Surface-Enhanced Raman Scattering (SERS) with the Surface Density of Gold Nanoparticles: Evaluation of the Critical Number of SERS Tags for a Detectable Signal. *Beilstein J. Nanotechnol.* **2019**, *10*, 1016−1023.
(35) Draine, B. T.; Flatau, P. J. User Guide for the Discrete Dipole Approximation Code DDSCAT 7.3. **2013**, arXiv:1305.6497.
(36) Draine, B. T.; Flatau, P. J. Discrete-Dipole Approximation for Scattering Calculations. *J. Opt. Soc. Am. A* **1994**, *11*, 1491−1499.
(37) Goodman, J. J.; Flatau, P. J.; Draine, B. T. Application of Fast-Fourier-Transform Techniques to the Discrete-Dipole Approximation. *Opt. Lett.* **1991**, *16*, 1198−1200.
(38) Olmon, R. L.; Slovick, B.; Johnson, T. W.; Shelton, D.; Oh, S.-H.; Boreman, G. D.; Raschke, M. B. Optical Dielectric Function of Gold. *Phys. Rev. B* **2012**, *86*, 235147.
(39) Kreibig, U.; Vollmer, M. *Optical Properties of Metal Clusters*; Springer: Berlin, 1995.
(40) Coletta, G.; Amendola, V. Numerical Modelling of the Optical Properties of Plasmonic and Latex Nanoparticles to Improve the Detection Limit of Immuno-Turbidimetric Assays. *Nanomaterials* **2021**, *11*, 1147.
(41) Rathnakumar, S.; Bhaskar, S.; Rai, A.; Saikumar, D. V. V.; Kambhampati, N. S. V.; Sivaramakrishnan, V.; Ramamurthy, S. S. Plasmon-Coupled Silver Nanoparticles for Mobile Phone-Based Attomolar Sensing of Mercury Ions. *ACS Appl. Nano Mater.* **2021**, *4*, 8066−8080.
(42) Doane, T. L.; Chuang, C.-H.; Hill, R. J.; Burda, C. Nanoparticle ζ-Potentials. *Acc. Chem. Res.* **2011**, *45*, 317−326.
(43) Biver, C.; Hariharan, R.; Mays, J.; Russel, W. B. Neutral and Charged Polymer Brushes: A Model Unifying Curvature Effects from Micelles to Flat Surfaces. *Macromolecules* **1997**, *30*, 1787−1792.
(44) Lee, S.-K.; Kim, H.-C.; Cho, S.-J.; Jeong, S. W.; Jeon, W. B. Binding Behavior of CRP and Anti-CRP Antibody Analyzed with SPR and AFM Measurement. *Ultramicroscopy* **2008**, *108*, 1374−1378.
(45) Luo, Y.; Wang, Y.; Liu, M.; Zhu, H.; Chen, O.; Zou, S.; Zhao, J. Colloidal Assembly of Au−Quantum Dot−Au Sandwiched Nanostructures with Strong Plasmon−Exciton Coupling. *J. Phys. Chem. Lett.* **2020**, *11*, 2449−2456.
(46) Poletti, A.; Fracasso, G.; Conti, G.; Pilot, R.; Amendola, V. Laser Generated Gold Nanocorals with Broadband Plasmon Absorption for Photothermal Applications. *Nanoscale* **2015**, *7*, 13702−13714.
(47) Bhaskar, S.; Das, P.; Moronshing, M.; Rai, A.; Subramaniam, C.; Bhaktha, S. B. N.; Ramamurthy, S. S. Photoplasmonic Assembly of Dielectric-Metal, Nd2O3-Gold Soret Nanointerfaces for Dequenching the Luminophore Emission. *Nanophotonics* **2021**, *10*, 3417−3431.
(48) Bhaskar, S.; Kowshik, N. C. S. S.; Chandran, S. P.; Ramamurthy, S. S. Femtomolar Detection of Spermidine Using Au Decorated SiO_2 Nanohybrid on Plasmon-Coupled Extended Cavity Nanointerface: A Smartphone-Based Fluorescence Dequenching Approach. *Langmuir* **2020**, *36*, 2865.
(49) Bhaskar, S.; Patra, R.; Kowshik, N. C. S. S.; Ganesh, K. M.; Srinivasan, V.; Chandran S, P.; Ramamurthy, S. S. Nanostructure Effect on Quenching and Dequenching of Quantum Emitters on Surface Plasmon-Coupled Interface: A Comparative Analysis Using Gold Nanospheres and Nanostars. *Phys. E* **2020**, *124*, 114276.

https://doi.org/10.1021/acsanm.1c03380
ACS Appl. Nano Mater. 2022, 5, 578−586